



HAL
open science

X-Ray diffraction study of oxygen deficient $Y_{2}Ti_{2}O_{7-\delta}$ pyrochlore powders synthesized by high-energy ball milling (HEBM)

Guillaume Josserand, Laurent Chaffron, Joel Ribis, Pierre-Francois Giroux,
Thierry Gloriant, David Simeone

► To cite this version:

Guillaume Josserand, Laurent Chaffron, Joel Ribis, Pierre-Francois Giroux, Thierry Gloriant, et al.. X-Ray diffraction study of oxygen deficient $Y_{2}Ti_{2}O_{7-\delta}$ pyrochlore powders synthesized by high-energy ball milling (HEBM). Journal of Solid State Chemistry, 2022, 315, pp.123446. 10.1016/j.jssc.2022.123446 . cea-03773105

HAL Id: cea-03773105

<https://cea.hal.science/cea-03773105>

Submitted on 25 Nov 2022

HAL is a multi-disciplinary open access archive for the deposit and dissemination of scientific research documents, whether they are published or not. The documents may come from teaching and research institutions in France or abroad, or from public or private research centers.

L'archive ouverte pluridisciplinaire **HAL**, est destinée au dépôt et à la diffusion de documents scientifiques de niveau recherche, publiés ou non, émanant des établissements d'enseignement et de recherche français ou étrangers, des laboratoires publics ou privés.

X-ray diffraction study of oxygen deficient $Y_2Ti_2O_{7-\delta}$ pyrochlore powders synthesized by high-energy ball milling (HEBM)

Guillaume Josserand^{a*}, Laurent Chaffron^a, Joël Ribis^a,
Pierre-François Giroux^a, Thierry Gloriant^b, David Simeone^a

^a *Université Paris Saclay, CEA, Service de Recherches Métallurgiques
Appliquées, 91191 Gif-sur-Yvette, France*

^b *Univ Rennes, INSA Rennes, CNRS, ISCR-UMR 6226, F-35000 Rennes, France*

*Corresponding author. Email address: guillaume.josserand@cea.fr
Phone number : +33 1 69 08 33 34

Abstract

$Y_2Ti_2O_7$ pyrochlore are widely used for various applications, from oxygen transport to materials strengthening. Ultra-pure oxygen deficient $Y_2Ti_2O_{7-\delta}$ pyrochlore powders synthesized by high-energy ball milling (HEBM) are studied by X-ray diffraction (XRD). Rietveld analysis of diffraction patterns reveals that a large oxygen sub-stoichiometry can be accommodated in this material with only minor structural changes. This accommodation results from the ability of Ti ions to change their valence state, which is confirmed by complementary EELS analysis. It may also explain why $Y_2Ti_2O_7$ is both radiation and mechanical milling resistant. This work highlights the fact that selection of cations allows rigid ionic structures like pyrochlore to accommodate a large amount of point defects.

Keywords: oxygen-deficient pyrochlore, X-ray diffraction, defective ionic structure

1. Introduction

The pyrochlore oxides of general formula $A_2B_2O_7$ are extensively used in the industry. Because of the diversity of elemental composition and their high density

of anionic defects, pyrochlore oxides find many applications such as cathode and solid electrolyte for fuel cells, ceramics for nuclear waste conditioning, dielectric, piezoelectric, ferro- and ferrimagnetic components, semiconductors, high refractive index optical elements, thermal and environmental barrier coatings, or catalysts [1-7]. Due to their irradiation and coarsening resistance, $Y_2Ti_2O_7$ pyrochlore nanoparticles are also successfully used as reinforcement for Oxide Dispersion Strengthened (ODS) ferritic steels [8, 9]. In ODS steels, these nanoparticles are incorporated in the metal powder grains through mechanical alloying. They produce a nano-precipitation that significantly improves the mechanical properties of the ferritic alloys, especially creep lifetime [10].

Synthesis of $Y_2Ti_2O_7$ pyrochlore phase can be achieved through different ways: mechanochemical synthesis, hydrothermal and solvothermal processes, Pechini type route, polymerized sol-gel or coprecipitation [7, 11-16]. HEBM of Y_2O_3 and TiO_2 precursors, followed by a thermal annealing appears to be a promising elaboration route as it is a simple, economical, and solvents-free method [11, 17]. However, defects induced by this solid-state way are often considered difficult to analyze and even more to quantify [18, 19].

The aim of this work is to examine the nature of defects and to study the structural stability of oxygen-deficient $Y_2Ti_2O_{7-\delta}$ nano-particles by X-ray diffraction. The material processing and experimental characterizations are first described, before presenting the results of diffraction patterns refinements. Finally, the stability of oxygen-deficient $Y_2Ti_2O_{7-\delta}$ pyrochlore is discussed.

2. Material processing and experimental characterizations

The crystalline structure of the ideal pyrochlore phase and the mechanosynthesis process are briefly described before discussing the annealing conditions of $Y_2Ti_2O_7$ nanoparticles.

2.1. The $Y_2Ti_2O_7$ pyrochlore structure

Ideal pyrochlore structure can be defined as a lacunar and twice ordered fluorite structure, following the general formula $A_2B_2O_6O'$. The cubic lattice of space group $Fd\bar{3}m$ consists of eight face-centered cubic sub-lattices, *i.e.* 88

atoms. There are four unique atomic positions and, by fixing the origin at the B site (origin choice 1 in crystallographic international tables), the atoms have the following Wyckoff positions : A at 16d (1/2, 1/2, 1/2), B at 16c (0, 0, 0), O at 48f (x, 1/8, 1/8) and O' at 8b (3/8, 3/8, 3/8).

Fig. 1 displays the different coordination polyhedra describing the $Y_2Ti_2O_7$ pyrochlore structure: six oxygen anions occupy the 48f position and are bound to two Y cations and two Ti cations, while the seventh oxygen is surrounded by four Y cations in position 8b. An ordered vacancy lies at position 8a, the tetrahedral site formed by four Ti cations. Yttrium is therefore coordinated to eight oxygen atoms (green distorted cubes in Fig. 1) and titanium to six oxygen atoms (blue distorted octahedra in Fig. 1) [20].

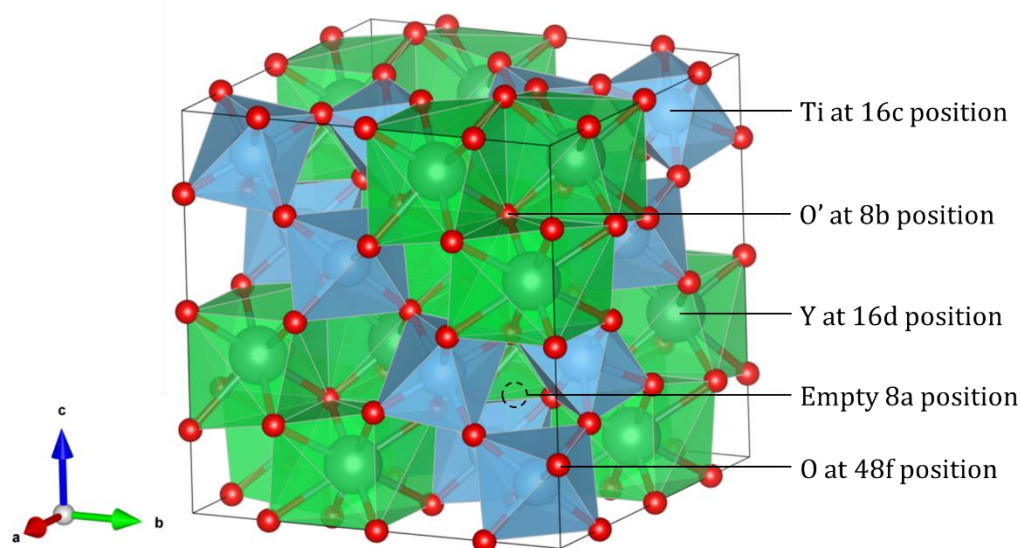


Figure 1: $Y_2Ti_2O_7$ ideal pyrochlore structure. Green distorted cubes and blue distorted octahedra correspond to Y and Ti cations coordination environments, respectively. (2-column fitting figure, color should be used)

2.2. Mechanosynthesis and thermal annealing

$Y_2Ti_2O_{7-\delta}$ pyrochlore nanostructured powder is obtained by HEBM of Y_2O_3 and TiO_2 precursors, followed by a thermal annealing. In order to remove surface adsorbed species, precursor nanopowders Y_2O_3 (Sigma-Aldrich, 99.9%) and TiO_2 (Degussa, 99.5%) foremost undergo a 10 hours long degassing under secondary

vacuum (10^{-6} mbar) at 1000°C and 500°C , respectively. Powders are then stored under a protective argon atmosphere to avoid any contamination. As described by Simondon et al. [11], three grams of a stoichiometric mixture $\text{Y}_2\text{O}_3 : 2\text{TiO}_2$ are placed in a modified Fritsch Pulverisette P_0 equipped with tungsten carbide vial and ball. A 120 hours milling is performed under static vacuum at a specific milling intensity of $1400\text{m}\cdot\text{s}^{-2}$ [21]. After ball milling, powders are stored in a glove box under high purity Ar atmosphere (99.995%). During milling process, WC vial and ball react with the powders and reduce them via a solid-state reaction, as previously reported [22, 23]. Rietveld refinement of XRD patterns of pyrochlore powders annealed 1 min at 900°C under vacuum revealed a high sub-stoichiometry in oxygen (not shown here). It was then decided to anneal them under oxygen atmosphere. To perform the heat-treatment, powders are placed in an alumina container disposed in a quartz tube. A secondary vacuum (10^{-6} mbar) is carried out at room temperature before setting an oxygen atmosphere ($p_{\text{O}_2} = 1$ atm) supplied by a pure O_2 flow (99.995% purity, 10 l/h). Crystallization of the desired phase occurring around 850°C [11], it has been chosen to perform heat treatments just above and at higher temperature, *i.e.* 900°C and 1050°C , respectively. Annealing were conducted during various duration, from one to 1200 minutes. The heating rate is fixed at $10^{\circ}\text{C}/\text{min}$. The different thermal treatments are summarized in Table 1.

Powder	Atmosphere	Annealing temperature ($^{\circ}\text{C}$)	Annealing time (min)
900_1	$p_{\text{O}_2} = 1$ bar	900	1
900_10			10
900_120			120
900_300			300
900_600			600
900_1200			1200
1050_1			$p_{\text{O}_2} = 1$ bar
1050_10	10		
1050_120	120		
1050_300	300		
1050_600	600		
1050_1200	1200		

Table 1: Annealing conditions of the different milled powders.

2.3. Characterization

$Y_2Ti_2O_{7-\delta}$ nanostructured powders are characterized after thermal annealing. The characteristic size and shape of nanoparticles are determined using Transmission Electronic Microscopy (TEM). X-ray powder diffraction technique is also used to analyze the crystalline structure of $Y_2Ti_2O_{7-\delta}$.

2.3.1. TEM

Nanometric crystallites of annealed powders are observed by TEM. Aggregates are briefly grinded in an agate mortar and set on a 3 mm copper mesh coated by a carbon film. Images are acquired with a JEOL 2010-F operating at 200 kV coupled with a Gatan Orius SC600A CCD camera. Oxidation state of *Ti* cations are determined by electron energy-loss spectroscopy (EELS) using a dual-corrected JEOL neoARM operated at 200 kV and equipped with a Continuum Gatan Image Filter (GIF).

2.3.2. X-ray diffraction setup and refinement

X-ray diffraction diagrams are collected on a Bruker D8 Advance (250 mm goniometer) using a Cu K_α (1.54056 Å) source operating at 40 kV and 40 mA. A primary slit of 0.1 mm width has been used for collimating the incident beam. A positioning sensitive detector (Vantec) was used to collect intensities during 2θ scans on the range 20°-120°. The angular step and the step time were kept constant and equal to 0.02° and 4 seconds, respectively. These set-up allows to maximize the signal-to-noise ratio and insures an accurate definition of Bragg peaks (>10 points/peak). Optical aberrations of the X-ray setup have been previously studied [24] and were used to analyse diffraction patterns. In order to extract information on the atomic structure and the microstructure, Le Bail and Rietveld refinements have been performed on collected diffraction patterns, using the Jana2006 software [25]. Weighted and Bragg reliability factors were all below 10% (see Tables 2 and 3). The flat backgrounds are approximated by a Legendre polynomial of degree five. The shape of Bragg peaks were fitted by pseudo-Voigt profiles. A Cagliotti function has been extracted from the analysis of diffraction patterns collected on a LaB_6 NIST sample for the X-ray setup.

3. Results

3.1. Crystalline nature of annealed nanoparticles

Fig. 2 displays the XRD diagrams acquired on the powder annealed at 1050°C during 600 minutes. All Bragg peaks of the diffraction patterns can be indexed by the $Fd\bar{3}m$ space group, regardless of the heat treatment performed and in agreement with the expected pyrochlore structure. No extra Bragg peaks associated with either tetragonal or orthorhombic TiO_2 or cubic or monoclinic Y_2O_3 were observed. Table 2 summarizes information extracted from the analysis of diffraction patterns for all samples. Information on the chemical reaction is given by measurement of the scale factor, which does not vary. This insures that no amorphous phase exists, corroborating the solid-solid chemical reaction is achieved at the chosen temperatures.

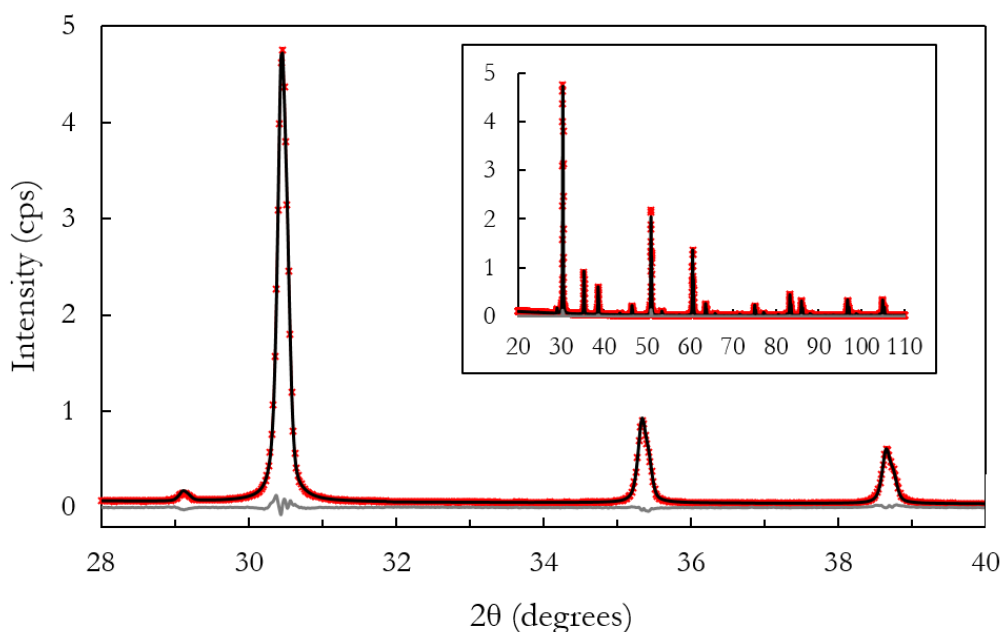


Figure 2: Zoom showing the comparison between the experimental (red cross) and refined (black line) diffraction pattern with associated errors (grey line) collected on sample annealed 600 minutes at 1050°C. The inset displays the full diagram with the refinement and associated errors. The quality of the refinement is justified by the very good agreement between the measured and computed patterns. (2-column fitting figure, color should be used)

Powder	Scale factor (10^{-3})	R_{wp} (%)	CDD (nm)	$\langle\sqrt{\varepsilon^2}\rangle$ (10^{-4})	Lattice parameter (\AA)	TEM mean crystallite size (nm)
900_1	1.399 (16)	9.89	94 (28)	29.94 (3.61)	10.11272 (144)	62 (10)
900_10	1.328 (12)	8.12	103 (6)	23.29 (3.02)	10.10338 (224)	-
900_120	1.490 (11)	8.35	111 (17)	17.24 (1.51)	10.09634 (62)	-
900_300	1.149 (7)	8.03	90 (8)	10.45 (1.04)	10.09472 (42)	-
900_600	1.394 (6)	6.46	89 (4)	7.11 (52)	10.09266 (21)	74 (15)
900_1200	1.414 (7)	7.48	106 (9)	11.17 (84)	10.09389 (34)	-
1050_1	1.271 (6)	6.85	89 (6)	9.08 (71)	10.09528 (29)	-
1050_10	1.414 (7)	2.94	100 (5)	7.10 (67)	10.09462 (54)	-
1050_120	1.483 (7)	6.86	128 (9)	6.97 (52)	10.09123 (22)	-
1050_300	1.157 (4)	6.22	98 (5)	5.94 (44)	10.09367 (18)	-
1050_600	1.427 (7)	6.88	135 (10)	5.05 (45)	10.09332 (44)	137 (66)
1050_1200	1.393 (3)	7.09	110 (11)	4.82 (82)	10.09329 (34)	-

Table 2: Various values related to the different $Y_2Ti_2O_{7-\delta}$ powders from XRD diagrams analysis: scale factor, weighted reliability factor, coherent diffracting domains size, micro-strains and lattice parameter, as well as the mean crystallite size measured on TEM micrographs. Associated errors are the standard uncertainties computed by Jana2006.

3.2. Crystallites size and micro-strains

TEM micrographs of three annealed powders are presented in Fig. 3. Aggregates of 900_1 powder are made of poorly defined grains (Fig. 3a), whereas polygonalization and slight growth occur with dwelling time (900_600, Fig. 3b)

and temperature (1050_600, Fig. 3c). The crystallites exhibit a roughly spherical shape, and their size is about 100 nm as mentioned in Table 2.

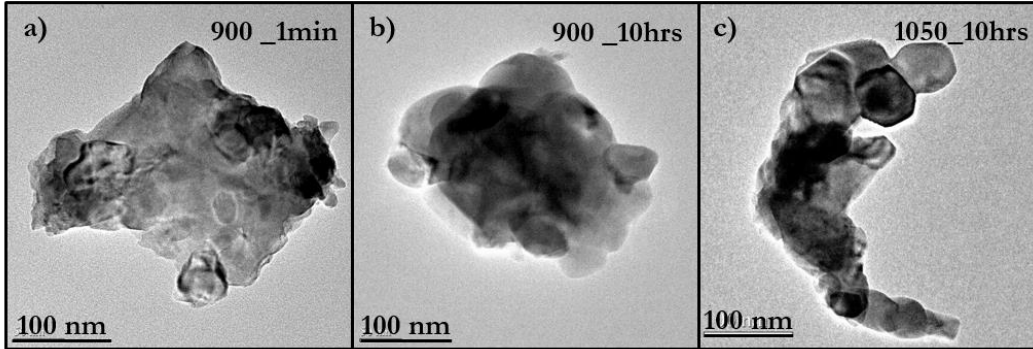


Figure 3: TEM micrographs of 900_1, 900_600 and 1050_600 annealed particles. Increasing the annealing time, grains become spherical. (2-column fitting figure)

XRD peaks widening gives complementary information on the pyrochlore microstructure. The size of coherent diffraction domains (CDD), L , and the micro-deformation $\langle\sqrt{\varepsilon^2}\rangle$ can be determined by the Lorentzian component of the pseudo-Voigt peaks profile; the Gaussian component is due to instrumental widening described by the Cagliotti function. As TEM observations prove the grains are spherical, the classical Hall-Williamson (HW) analysis can be performed on the Lorentzian component of pseudo-Voigt profiles [26]:

$$\beta_{hkl} \cdot \cos \theta_{hkl} = \lambda/L + 2\langle\sqrt{\varepsilon^2}\rangle \sin \theta_{hkl} \quad (1)$$

where β_{hkl} is the full width at middle height (FWMH) of the Lorentzian component of the hkl Bragg peak, L is the characteristic size of the CDD, and $\langle\sqrt{\varepsilon^2}\rangle$ can be understood as the root mean square of the micro-strain in the material, *i.e.* the average deviation of the interplanar distances d_{hkl} to their mean value.

Numerical values of both L and $\langle\sqrt{\varepsilon^2}\rangle$ are reported in Table 2. The characteristic sizes of CDD extracted from X-ray refinements are nanometric for all the synthesized powders, with a size from 89 (8) nm to 134 (10) nm. These results are of the same order of magnitude than the mean crystallite size determined by TEM observations. This implies that L can be understood as a grain size. As shown in Fig. 4a, the coarsening rate of the CDD is higher at 1050°C than at 900°C, but is still moderate. This is consistent with the exceptional coarsening

resistance of $Y_2Ti_2O_7$ nano-features observed in ODS steels up to 1100°C [27]. The heat-treatment performed are therefore suitable to produce nanostructured materials and avoid major coarsening.

The root mean square of the micro-strain $\langle\sqrt{\varepsilon^2}\rangle$ is divided by 4 with the annealing time at 900°C and by 2 at 1050°C (see Fig. 4 and Table 2). Extended annealing time leads to a better ordering of crystallites structure, in accordance with both TEM observations and a conventional pattern of stress relaxation. The decreasing of $\langle\sqrt{\varepsilon^2}\rangle$ with the annealing time may also be due to the time-dependency of the diffusion of defects in the material. The vanishing of defects under an oxygen partial pressure of one atmosphere is probably due to the oxidation of the pyrochlore powders. The vacancy concentration decreases as the oxygen atoms penetrate inside the material, and the inter-reticular distance d_{hkl} tends to reach a unique value.

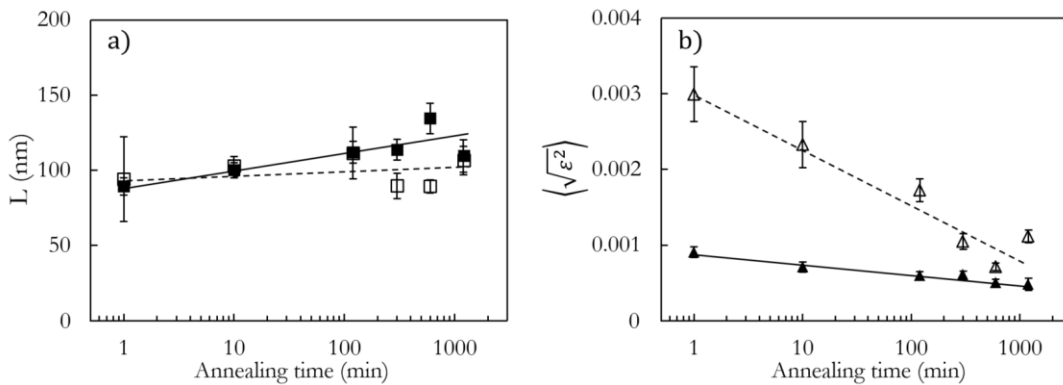


Figure 4: Evolution of CDD (a) and micro-strains (b) extracted from the HW analysis with annealing time. Powders annealed at 900°C (open symbols and dashes) exhibit larger variations in micro-strains than those treated at 1050°C (black symbols and full line). Only slight coarsening is observed with time for both of the annealing temperature. (2-column fitting figure)

3.3. Evolution of the unit cell parameter

The position of different Bragg peaks, corrected from the positioning misfit, allows to compute the evolution of the unit cell parameter, a , of the pyrochlore structure. Fig. 5 displays the variation of a with annealing time. As shown in Fig. 5, powders annealed at 900°C exhibit wide variations from 10.11272 (144) Å to 10.09266 (21) Å, for 900_1 and 900_600, respectively (see Table 2). From 1 to 120 minutes, the lattice parameter decreases linearly with the logarithm of time.

However, this trend does not fit anymore for the sample annealed 300 minutes and more, suggesting that a steady state was reached. Samples heat-treated at 1050°C exhibit only a slight decrease of the lattice parameter with time, from 10,09528 (29) Å for 1050_1 to 10,09329 (34) Å for 1050_1200.

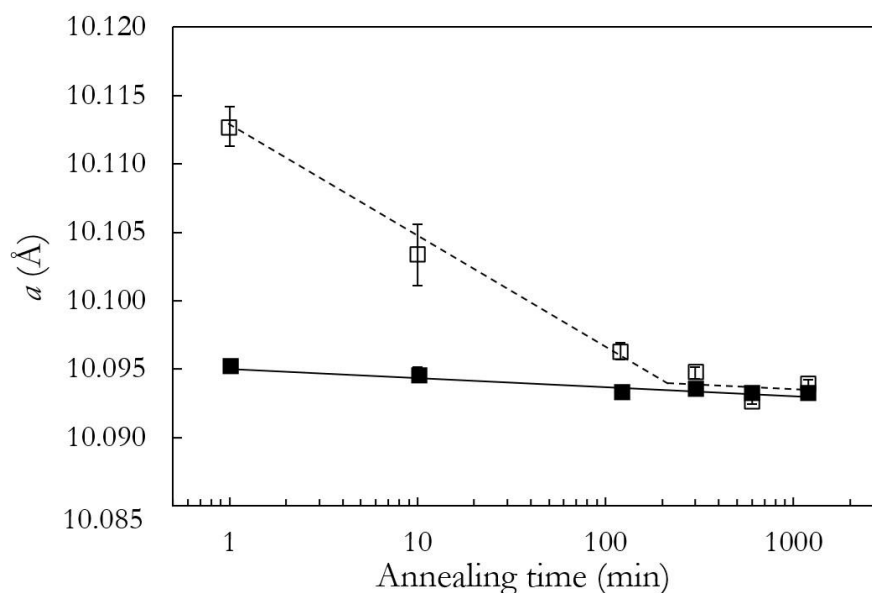


Figure 5: Evolution of the unit lattice parameter with annealing time at 900°C (open squares and dashes) and 1050°C (black squares and full line). Errors bars associated with the evolution of a are also plotted. (1-column fitting figure)

3.4. Variations of oxygen position and stoichiometry

To go at step beyond, Rietveld refinements were performed to follow the evolution of structural parameters, *i.e.* position and occupancy rate of atoms constituting the pyrochlore structure, as a function of the annealing time and temperature. As we are concerned by an oxygen diffusion mechanism, attention has been concentrated on the position and the occupancy of oxygen atoms along the $48f$ and $8a$ Wyckoff positions. Refinements performed assuming vacancies in the $8a$ sites are always unstable, so their occupancy rate has been constrained to be fully occupied. This work focuses here on the O_{48f} position, which includes 6 of the 7 oxygen atoms and is therefore the main source of anionic vacancies and oxygen mobility [20, 28]. The quality of the Rietveld refinements is assessed by

the low values of R_{Bragg} factor that remains lower than 10% as reported in Table 3.

Fig. 6 displays the evolution of the reduced atomic position of the 48*f* oxygen atoms, defined by x (Fig. 6a), and their sub-stoichiometry δ , (Fig. 6b). Numerical values are also reported in Table 3. Fig. 6a reveals that at 1050°C, x (black squares) remains almost constant and equal to 0.332. This result is in agreement with previous investigations at equilibrium state [29, 30]. At lower temperature, we observe a large decreasing of x (open squares) with the annealing time from 0.3525(31) to 0.3332(7), for 900_1 and 900_600, respectively. Only large annealing time (>300 min) allows reaching the expected equilibrium value of x . Fig. 6b shows that the oxygen sub-stoichiometry δ in the pyrochlore structure strongly depends on the annealing time and temperature. The oxidizing atmosphere ($p_{O_2} = 1$ atm) decreases the density of 48*f* vacancies due to the diffusion of oxygen in the lattice. Oxygen sub-stoichiometry δ ranges from 1.59(19) to 0.01(10) for 900_1 and 1050_1200, respectively. The sub-stoichiometry linearly decreases with the logarithm of time at fixed temperatures (Fig. 6b). Adjusting annealing time and temperature under oxygen atmosphere is therefore a simple and efficient way to tune the oxygen stoichiometry of $Y_2Ti_2O_{7-\delta}$ nanostructured powders on a wide range.

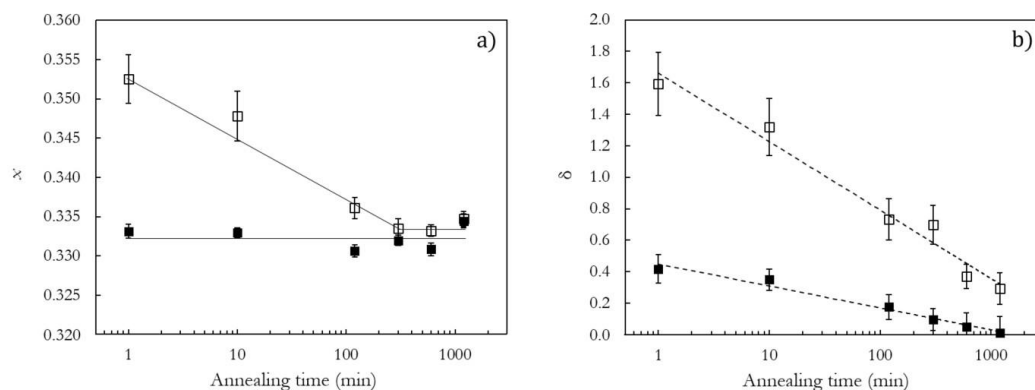


Figure 6: Evolution of the reduced atomic position x (a) and oxygen sub-stoichiometry δ (b) in $Y_2Ti_2O_{7-\delta}$ powders annealed under oxygen flow at 900°C (open symbols) and 1050°C (black symbols). (2-column fitting image)

Powder	R_{Bragg} (%)	δ	x	$ TiO_{48f} $ (Å)	$ YO_{48f} $ (Å)
900_1	8.06	1.59 (19)	0.3525 (31)	2.06653 (30)	2.32820 (40)

900_10	5.68	1.32 (18)	0.3478 (32)	2.0412 (50)	2.3566 (50)
900_120	5.24	0.73 (13)	0.3361 (14)	1.98522 (12)	2.43390 (15)
900_300	5.30	0.70 (12)	0.3335 (13)	1.97357 (8)	2.45142 (10)
900_600	3.84	0.37 (8)	0.3332 (7)	1.97186 (4)	2.45304 (5)
900_1200	5.22	0.29 (10)	0.3347 (10)	1.97869 (8)	2.44282 (6)
1050_1	4.93	0.42 (9)	0.3331 (9)	1.97214 (6)	2.45404 (8)
1050_10	4.82	0.35 (7)	0.3330 (6)	1.97143 (4)	2.45534 (5)
1050_120	6.41	0.18 (8)	0.3306 (7)	1.96065 (4)	2.47057 (5)
1050_300	4.63	0.10 (7)	0.3319 (6)	1.96642 (4)	2.46244 (5)
1050_600	6.17	0.05 (9)	0.3308 (8)	1.96161 (4)	2.46966 (5)
1050_1200	5.13	0.01 (10)	0.3344 (9)	1.97752 (4)	2.44461 (5)

Table 3: Various values related to the different $Y_2Ti_2O_{7-\delta}$ powders extracted from Rietveld refinements: R_{Bragg} factor, oxygen sub-stoichiometry (δ), x parameter and cation-oxygen 48f bond lengths. Associated errors are the standard uncertainties computed by Jana2006.

4. Discussion

In order to study in detail the evolution of the structure with the oxygen stoichiometry, the variation of the unit cell parameter a as a function of δ is plotted in Fig. 7. At very high sub-stoichiometry ($\delta > 1.0$), a is larger than the expected value for $Y_2Ti_2O_7$ pyrochlore (ca. 10.095 Å [1, 12]). For smaller δ value ($\delta < 1$), the unit cell only slightly vary.

The nonlinear evolution of a as a function of δ may be explained by a simple analysis of the oxidation state of Ti cations. Y is well known for having a single and constant 3+ oxidation state, in contrast to Ti ions whose valence varies from 2+ to 4+. For $\delta < 1.0$, it is possible to determine the fraction of Ti^{3+} ions in the materials from electro-neutrality. The atomic fraction of Ti^{3+} , $\alpha = [Ti^{3+}]/[Ti]$ (where $[X]$ is the atomic fraction of species X) satisfies:

$$2 \times 3 + 2 \times (3\alpha + 4(1 - \alpha)) - (7 - \delta) \times 2 = 0 \quad (2)$$

In this equation, the oxidation states of Y and O are considered constant and equal to 3+ and 2-, respectively. α results from the existence of oxygen vacancies in the neighborhood of Ti ions that modify the oxidation state of Ti ions. From the knowledge of α , the mean ionic radius of Ti , resulting from different oxidation states can be computed from Shannon radii [31] :

$$\langle r \rangle = r_{Ti^{3+}} \times \alpha + r_{Ti^{4+}} \times (1 - \alpha) \quad (3)$$

Assuming that the oxygen O^{2-} radius is fixed [31], the mean $Ti - O$ distance is equal to $r_{O^{2-}} + \langle r \rangle$. As the oxygen sub-stoichiometry increases, both the mean radius of Ti and the reduced atomic position of the oxygen x increase due to electrostatic repulsion. The transition from Ti^{4+} to Ti^{3+} induces not only a variation of the mean Ti radius, but also a slight increase of the oxygen reduced atomic position x in the unit cell of the pyrochlore structure as displayed in Fig. 7 and 8. For $\delta > 1.0$, the electro-neutrality implies that the mean oxidation state of Ti ions is lower than 3+, leading to the vanishing of Ti^{4+} ions and the formation of Ti^{2+} cations. The ionic radius of Ti^{2+} ions (860 pm) is much larger than those associated with Ti^{3+} (670 pm) and Ti^{4+} (605 pm) [31]. To keep the octahedral environment, x and a must both strongly increase to compensate for the large Ti^{2+} radius, as illustrated in Fig. 8. Ti cations have a variable oxidation state but are able to keep the same octahedral coordination environment. This configuration justifies the ability of the pyrochlore structure to accommodate anionic vacancies on a large range ($0.0 < \delta < 2.0$).

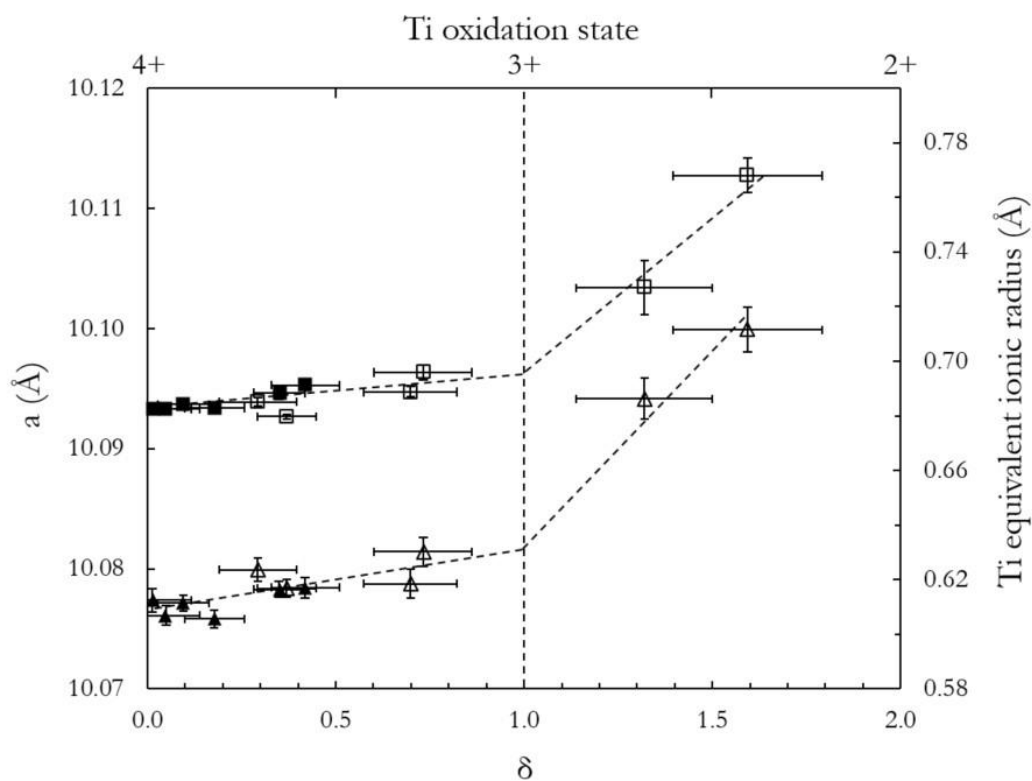


Figure 7: Increasing of lattice parameter a (squares) and Ti ionic radius (triangles) with oxygen sub-stoichiometry (δ), due to Ti oxidation state variations in $Y_2Ti_2O_{7-\delta}$ powders annealed at 900°C (open symbols) and 1050°C (black symbols). (1-column fitting figure)

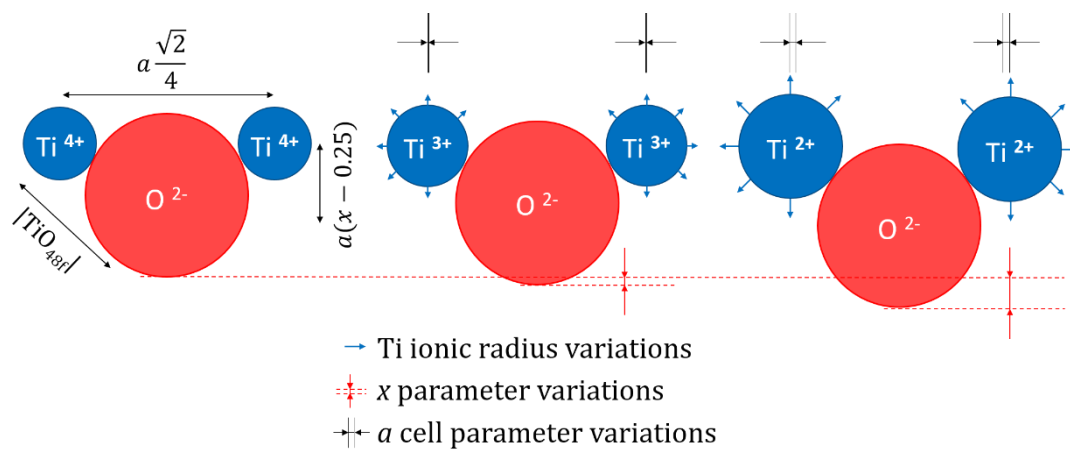


Figure 8: Schematic description of the variations of the reduced atomic position x , unit cell parameter a and Ti–O distance induced by changing Ti oxidation state in a sub-stoichiometric pyrochlore structure. Atoms are roughly on scale. (2-column fitting figure, color to be used)

To confirm the presence of reduced *Ti* cations, the 900_1 sample is analyzed by EELS. This technique of spectroscopy is able to distinguish the valence of ions constituting the nanostructured powders. Spectra focused on the *Ti-L_{3,2}* and *O-K* edges are acquired on several aggregates. As shown on Fig 9, *Ti-L_{3,2}* and *O-K* edges are clearly identified on the background-subtracted EELS spectra. Some aggregates of 900_1 powder exhibits Ti^{4+} ions, clearly identified as the *Ti-L_{3,2}* edges are subdivided [32, 33]. Other aggregates in the same powder display *Ti* reduced cations as shown on Fig 9. *Ti-L_{3,2}* edges of reduced ions are single peaks, slightly shifted towards lower energy-loss [32]. It is difficult to determine if the EELS spectra is the signature of Ti^{2+} , Ti^{3+} or a convolution, as their EELS profiles are very similar [32, 33]. The *O-K* edge splitting attenuation may indicate a predominance of Ti^{3+} [33]. In any case, EELS analysis confirms the presence of reduced *Ti* ions predicted by the XRD Rietveld refinements. The inhomogeneity of the powder revealed by EELS is probably due to its out-of-equilibrium state. This may explain why the most sub-stoichiometric powders have larger uncertainties about the various data extracted from XRD refinements.

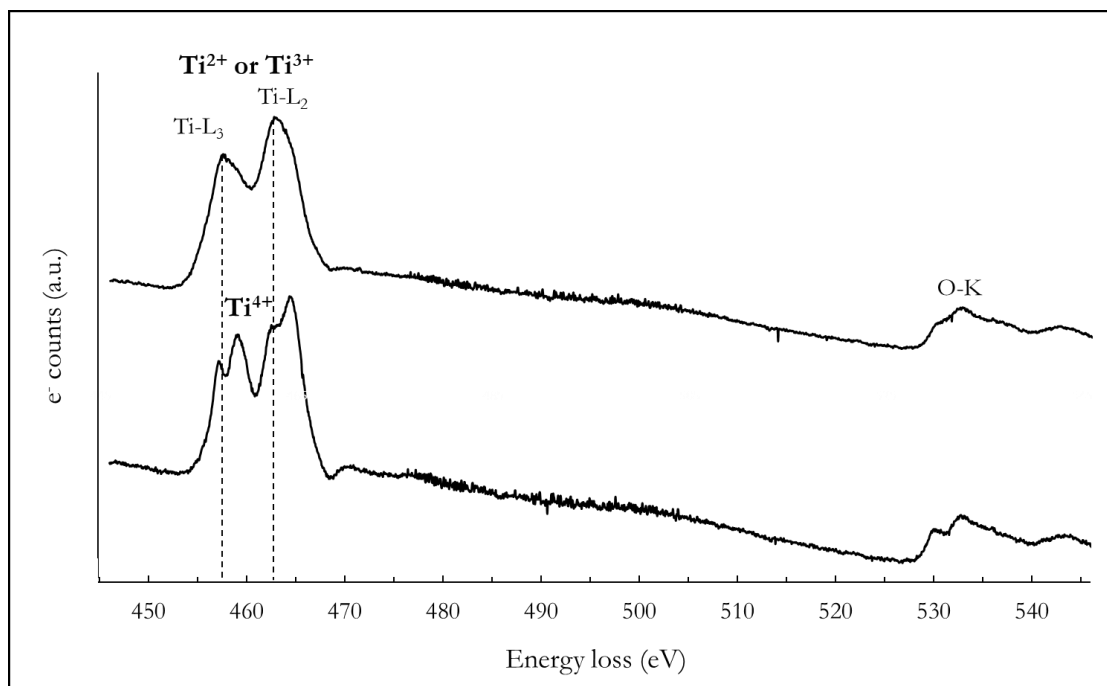


Figure 9: Background-subtracted EELS spectra focused on $Ti-L_{2,3}$ and $O-K$ edges acquired in the same conditions on two different aggregates of 900_1 $Y_2Ti_2O_{7-\delta}$ pyrochlore powder. Reduced Ti (up) and Ti^{4+} (bottom) cations are identified. (2-column fitting figure)

5. Conclusion

In this work, the evolution of the oxygen deficient $Y_2Ti_2O_{7-\delta}$ resulting from HEBM was studied with X-ray diffraction technique. The Rietveld method has been applied on the diffraction patterns collected on pyrochlore powders annealed in various conditions under an oxidizing atmosphere. The analysis of these diagrams provides quantitative information, not only on the microstructure but also on the atomic structure of this material as a function of the oxygen sub-stoichiometry. The Rietveld analysis proves that the concentration of point defects on the $48f$ position decreases with annealing time at a given temperature, as expected for a diffusional process. Structural information derived from refinements highlights that this oxidation process is associated with a change in the Ti valence confirmed by EELS analysis. The link between oxygen substoichiometry and Ti oxidation state is explained, and thresholds have been determined:

- For $0.0 < \delta < 1.0$ the oxidation state of Ti varies from +4 to +3 and induces only slight variations in the pyrochlore cell structure;
- As soon as $1.0 < \delta < 2.0$, the appearance of large Ti^{2+} cations leads to important deformations of coordination environment, and an increase in the unit cell parameter and the reduced atomic position. The coordination environment of Ti cation is notwithstanding conserved, ensuring the stability of the pyrochlore phase.

The main result of this work is to show that even for crystalline structure made of rigid building blocks like pyrochlore, a large amount of oxygen vacancies can be accommodated. The negligible variation of the unit cell parameter for a large sub-stoichiometric range may explain the stability of this particular pyrochlore under extreme solicitations, such as HEBM and irradiation [34, 35]. The ability of such pyrochlore for accommodating a large amount of oxygen vacancies might also find various applications in nuclear waste immobilization [36, 37] and oxygen catalyts and transport [3-5, 38, 39].

Acknowledgements

The authors would like to thank E. Bouaravong for the help provided on powders synthesis and characterization.

CRedit author statement

Guillaume Josserand: Investigation, Writing – Original Draft, Laurent Chaffron: Conceptualization, Methodology, Joël Ribis: Investigation, Pierre-François Giroux: Conceptualization, Supervision, Thierry Gloriant: Supervision, David Simeone: Methodology, Writing - Reviewing and Editing

References

- [1] M. Subramanian, G. Aravamudan, G. S. Rao, Oxide pyrochlores—a review, *Progress in Solid State Chemistry* 15 (2) (1983) 55–143.
[https://doi.org/10.1016/0079-6786\(83\)90001-8](https://doi.org/10.1016/0079-6786(83)90001-8)
- [2] B. J. Wuensch, K. W. Eberman, C. Heremans, E. M. Ku, P. Onnerud, E. M. Yeo, S. M. Haile, J. K. Stalick, J. D. Jorgensen, Connection between oxygen-ion conductivity of pyrochlore fuel-cell materials and structural change with composition and temperature, *Solid State Ionics* 129 (1-4) (2000) 111–133.
[https://doi.org/10.1016/S0167-2738\(99\)00320-3](https://doi.org/10.1016/S0167-2738(99)00320-3)
- [3] M. Kim, J. Park, M. Kang, J. Y. Kim, S. W. Lee, Toward efficient electrocatalytic oxygen evolution: Emerging opportunities with metallic pyrochlore oxides for electrocatalysts and conductive supports, *ACS Central Science* 6 (6) (2020) 880–891.
<https://doi.org/10.1021/acscentsci.0c00479>
- [4] V. Sadykov, A. Shlyakhtina, N. Lyskov, E. Sadovskaya, S. Cherepanova, N. Ereemeev, V. Skazka, V. Goncharov, E. Kharitonova, Oxygen diffusion in Mg-doped Sm and Gd zirconates with pyrochlore structure, *Ionics* 26 (2020) 4621–4633.
<https://doi.org/10.1007/s11581-020-03614-5>

- [5] A. P. Anantharaman, H. P. Dasari, Potential of pyrochlore structure materials in solid oxide fuel cell applications, *Ceramics International* 47 (4) (2021) 4367–4388.
<https://doi.org/10.1016/j.ceramint.2020.10.012>
- [6] J. K. Gill, O. Pandey, K. Singh, Role of sintering temperature on thermal, electrical and structural properties of Y₂Ti₂O₇ pyrochlores, *International journal of hydrogen energy* 36 (22) (2011) 14943–14947.
<https://doi.org/10.1016/j.ijhydene.2011.02.138>
- [7] Z. Wang, X. Wang, G. Zhou, J. Xie, S. Wang, Highly transparent yttrium titanate (Y₂Ti₂O₇) ceramics from co-precipitated powders, *Journal of the European Ceramic Society* 39 (10) (2019) 3229–3234.
<https://doi.org/10.1016/j.jeurceramsoc.2019.04.018>
- [8] T. Liu, L. Wang, C. Wang, H. Shen, H. Zhang, Feasibility of using Y₂Ti₂O₇ nanoparticles to fabricate high strength oxide dispersion strengthened Fe–Cr–Al steels, *Materials & Design* 88 (2015) 862–870.
<https://doi.org/10.1016/j.matdes.2015.08.118>
- [9] E. Simondon, P.-F. Giroux, J. Ribis, G. Spartacus, L. Chaffron, T. Gloriant, Innovative method of ODS steels manufacturing by direct introduction of pyrochlore phase through milling, *Materials Characterization* (2021) 111461.
<https://doi.org/10.1016/j.matchar.2021.111461>
- [10] R. Klueh, P. Maziasz, I. Kim, L. Heatherly, D. Hoelzer, N. Hashimoto, E. Kenik, K. Miyahara, Tensile and creep properties of an oxide dispersion-strengthened ferritic steel, *Journal of Nuclear Materials* 307 (2002) 773–777.
[https://doi.org/10.1016/S0022-3115\(02\)01046-2](https://doi.org/10.1016/S0022-3115(02)01046-2)
- [11] E. Simondon, P.-F. Giroux, L. Chaffron, A. Fitch, P. Castany, T. Gloriant, Mechanical synthesis of nanostructured Y₂Ti₂O₇pyrochlore oxides, *Solid State Sciences* 85 (2018) 54–59.
<https://doi.org/10.1016/j.solidstatesciences.2018.09.006>
- [12] T. Gadipelly, A. Dasgupta, C. Ghosh, V. Krupa, D. Sornadurai, B. K. Sahu, S. Dhara, Synthesis and structural characterisation of Y₂Ti₂O₇ using microwave hydrothermal route, *Journal of Alloys and Compounds* 814

- (2020) 152273.
<https://doi.org/10.1016/j.jallcom.2019.152273>
- [13] D. Joseph, C. Kaliyaperumal, S. Mumoorthy, T. Paramasivam, Dependence on temperature of the electrical properties of nanocrystalline Y₂Ti₂O₇ ceramics, *Ceramics International* 44 (5) (2018) 5426–5432.
<https://doi.org/10.1016/j.ceramint.2017.12.172>
- [14] B. Milicevic, M. Marinovic-Cincovic, M. D. Dramicanin, Non-isothermal crystallization kinetics of Y₂Ti₂O₇, *Powder Technology* 310 (2017) 67–73.
<https://doi.org/10.1016/j.powtec.2017.01.001>
- [15] W. J. Lee, D. S. Bae, Synthesis and characterization of Y₂Ti₂O₇ photocatalytic powders by thermal assist process, in: *Defect and Diffusion Forum*, Vol. 380, Trans Tech Publ, 2017, pp. 86–91.
<https://doi.org/10.4028/www.scientific.net/DDE.380.86>
- [16] V. Chishkala, S. Lytovchenko, B. Mazilin, E. Gevorkyan, V. Shkuropatenko, V. Voyevodin, M. Rucki, Z. Siemiatkowski, J. Matijosius, A. Dudziak, et al., Novel microwave-assisted method of Y₂Ti₂O₇ powder synthesis, *Materials* 13 (24) (2020) 5621.
<https://doi.org/10.3390/ma13245621>
- [17] A. F. Fuentes, K. Boulahya, M. Maczka, J. Hanuza, U. Amador, Synthesis of disordered pyrochlores, A₂Ti₂O₇ (a= Y, Gd and Dy), by mechanical milling of constituent oxides, *Solid state sciences* 7 (4) (2005) 343–353.
<https://doi.org/10.1016/j.solidstatesciences.2005.01.002>
- [18] L. Takacs, Solid state reactions induced by ball milling, *Hyperfine Interactions* 111 (1) (1998) 245–250.
<https://doi.org/10.1023/A:1012670104517>
- [19] V. Sepelak, S. Bégin-Colin, G. Le Caer, Transformations in oxides induced by high-energy ball-milling, *Dalton Transactions* 41 (39) (2012) 11927–11948.
<https://doi.org/10.1039/C2DT30349C>
- [20] P. Wilde, C. Catlow, Defects and diffusion in pyrochlore structured oxides, *Solid State Ionics* 112 (3-4) (1998) 173–183.
[https://doi.org/10.1016/S0167-2738\(98\)00190-8](https://doi.org/10.1016/S0167-2738(98)00190-8)

- [21] Y. Chen, M. Bibole, R. Le Hazif, G. Martin, Ball-milling-induced amorphization in Ni_xZr_y compounds: A parametric study, *Physical Review B* 48 (1) (1993) 14.
<https://doi.org/10.1103/PhysRevB.48.14>
- [22] S. Begin-Colin, G. Le Caër, M. Zandona, E. Bouzy, B. Malaman, Influence of the nature of milling media on phase transformations induced by grinding in some oxides, *Journal of Alloys and Compounds* 227 (1995) 157-166.
[https://doi.org/10.1016/0925-8388\(95\)01596-5](https://doi.org/10.1016/0925-8388(95)01596-5)
- [23] T. Tao, A. M. Glushenkov, H. Hu, Q. Chen, Y. Chen, Ball milled SnO_2 : a modified vapor source for growing nanostructures, *Journal of Alloys and Compounds* 504S (2010) S315-318.
<https://doi.org/10.1016/j.jallcom.2010.02.193>
- [24] D. Simeone, G. Baldinozzi, D. Gosset, G. Zalczer, J. berar, Rietveld refinements performed on mesoporous ceria layers at grazing incidence, *J. Appl. Cryst.* 44 (0) (2011) 1205–1210.
<https://doi.org/10.1107/S0021889811042294>
- [25] V. Petricek, M. Dusek, L. Palatinus, Crystallographic computing system jana2006: general features, *Zeitschrift für Kristallographie-Crystalline Materials* 229 (5) (2014) 345–352.
<https://doi.org/10.1515/zkri-2014-1737>
- [26] G. Williamson, W. Hall, X-ray line broadening from filed aluminium and wolfram, *Acta metallurgica* 1 (1) (1953) 22–31.
[https://doi.org/10.1016/0001-6160\(53\)90006-6](https://doi.org/10.1016/0001-6160(53)90006-6)
- [27] M. Miller, K. Russell, D. Hoelzer, Characterization of precipitates in MA/ODS ferritic alloys, *Journal of nuclear Materials* 351 (1-3) (2006) 261–268.
<https://doi.org/10.1016/j.jnucmat.2006.02.004>
- [28] A. Krasnov, A. Kabanov, N. Kabanova, I. Piir, I. Shein, Ab initio modeling of oxygen ion migration in non-stoichiometric bismuth titanate pyrochlore $Bi_{1.5}Ti_2O_{6.25}$, *Solid State Ionics* 335 (2019) 135–141.
<https://doi.org/10.1016/j.ssi.2019.02.023>
- [29] L. Yang, Y. Jiang, G. R. Odette, W. Zhou, Z. Liu, Y. Liu, Nonstoichiometry and relative stabilities of $Y_2Ti_2O_7$ polar surfaces: A density functional theory

- prediction, *Acta materialia* 61 (19) (2013) 7260–7270.
<https://doi.org/10.1016/j.actamat.2013.08.031>
- [30] L. Minervini, R. W. Grimes, Y. Tabira, R. L. Withers, K. E. Sickafus, The oxygen positional parameter in pyrochlores and its dependence on disorder, *Philosophical Magazine A* 82 (1) (2002) 123–135.
<https://doi.org/10.1080/01418610208240001>
- [31] R. T. Shannon, C. Prewitt, Revised values of effective ionic radii, *Acta Crystallographica Section B: Structural Crystallography and Crystal Chemistry* 26 (7) (1970) 1046–1048.
<https://doi.org/10.1107/S0567740870003576>
- [32] B. Cao, K. Suenaga, T. Okazaki, H. Shinohara, Production, isolation, and EELS characterization of Ti₂@ C₈₄ dititanium metallofullerenes, *The Journal of Physical Chemistry B*, 106 (36) (2002) 9295–9298.
<https://doi.org/10.1021/jp026013b>
- [33] CN. Huang, JS. Bow, Y. Zheng, SY. Chen, N. Ho, P. She, Nonstoichiometric Titanium Oxides via Pulsed Laser Ablation in Water. *Nanoscale Research Letters* 5, (2010) 972–985.
<https://doi.org/10.1007/s11671-010-9591-4>
- [34] V. Badjeck, M. Walls, L. Chaffron, J. Malaplate, K. March, New insights into the chemical structure of Y₂Ti₂O₇- δ nanoparticles in oxide dispersion-strengthened steels designed for sodium fast reactors by electron energy-loss spectroscopy, *Journal of Nuclear Materials* 456 (2015) 292–301.
<https://doi.org/10.1016/j.jnucmat.2014.09.058>
- [35] F. Zhang, B. Manoun, S. Saxena, Pressure-induced order–disorder transitions in pyrochlore RE₂Ti₂O₇ (RE= Y, Gd), *Materials Letters* 60 (21–22) (2006) 2773–2776.
<https://doi.org/10.1016/j.matlet.2006.01.095>
- [36] S. Hayun, T. B. Tran, J. Lian, A. F. Fuentes, A. Navrotsky, Energetics of stepwise disordering transformation in pyrochlores, RE₂Ti₂O₇ (RE= Y, Gd and Dy), *Acta materialia* 60 (10) (2012) 4303–4310.
<https://doi.org/10.1016/j.actamat.2012.04.007>

- [37] L. Kong, Y. Zhang, I. Karatchevtseva, Preparation of Y₂Ti₂O₇ pyrochlore glass-ceramics as potential waste forms for actinides: the effects of processing conditions, *Journal of Nuclear Materials* 494 (2017) 29–36.
<https://doi.org/10.1016/j.jnucmat.2017.07.004>
- [38] Q. Feng, Z. Zhao, X.-Z. Yuan, H. Li, H. Wang, Oxygen vacancy engineering of yttrium ruthenate pyrochlores as an efficient oxygen catalyst for both proton exchange membrane water electrolyzers and rechargeable zinc-air batteries, *Applied Catalysis B: Environmental* 260 (2020) 118176.
<https://doi.org/10.1016/j.apcatb.2019.118176>
- [39] P. Wang, Q. Cheng, C. Mao, W. Su, L. Yang, G. Wang, L. Zou, Y. Shi, C. Yan, Z. Zou, et al., Regulation of oxygen vacancy within oxide pyrochlores by f-doping to boost oxygen-evolution activity, *Journal of Power Sources* 502 (2021) 229903.
<https://doi.org/10.1016/j.jpowsour.2021.229903>